Journal of Physics: Condensed Matter

PAPER

Exploration of high-pressure structural transition and electronic properties of $BaFe_2S_3$

To cite this article: Panlong Kong *et al* 2019 *J. Phys.: Condens. Matter* **31** 115401

IOP Publishing Journal of Physics: Condensed Matter
J. Phys.: Condens. Matter **31** (2019) 115401 (9pp) https://doi.org/10.1088/1361-648X/aaf8f8

Exploration of high-pressure structural transition and electronic properties of $BaFe_2S_3$

Panlong Kong[1,2,3], Jingjing Wang[4], Yuanyuan Jin[1], Chuanzhao Zhang[1], Cheng Lu[1,2,5], Yonghong Tian[1] and Haihua Chen[6]

[1] Department of Physics and Optoelectronic Engineering, Yangtze University, Jingzhou 434023, People's Republic of China
[2] Department of Physics, Nanyang Normal University, Nanyang 473061, People's Republic of China
[3] Center for High Pressure Science and Technology Advanced Research (HPSTAR), Beijing 100094, People's Republic of China
[4] Education College of Information Technology, Hubei Nomal University, Huangshi 435002, People's Republic of China
[5] School of Science, Northwestern Polytechnic University, Xi'an 710072, People's Republic of China
[6] Department of Basic Education, Qinghai University, Xining 810016, People's Republic of China

E-mail: lucheng@calypso.cn, yhtian@yangtzeu.edu.cn and chenghaihua06@163.com

Received 6 November 2018, revised 7 December 2018
Accepted for publication 17 December 2018
Published 22 January 2019

Abstract

The iron-based compound $BaFe_2S_3$ has received considerable attention in recent years due to its unique electronic properties with important applications. But, there has been relatively little attention devoted to the structure evolution of $BaFe_2S_3$ under high pressure. Here, we report a detailed theoretical study of the structural, electronic and sound velocity properties of $BaFe_2S_3$ under high pressure by CALYPSO structure search method in combination with the first-principles calculations. We have uncovered three novel structures of $BaFe_2S_3$ under high pressure with space group $P222_1$, $Imm2$, and $C2/m$ symmetries. Theoretical calculations reveal that the structures of $BaFe_2S_3$ under high pressure satisfy the phase transition sequence of $Cmcm \rightarrow P222_1 \rightarrow Imm2 \rightarrow C2/m$, and the corresponding transition pressures are 31.6, 47.4 and 57.0 GPa, respectively. Our results enrich the high pressure phases of $BaFe_2S_3$ and will stimulate future experiments to synthesize these new phases.

Keywords: high pressure, structural transition, $BaFe_2S_3$, first-principles calculations

Supplementary material for this article is available online

(Some figures may appear in colour only in the online journal)

1. Introduction

The iron-based compounds are one of the top research fields in the condensed matter physics, owing to their interesting physical properties and unique quasi 1D structure [1]. Great efforts have been made in studying the interplay among crystal structure, magnetism and superconductivity of the iron-based compounds [1–6]. Recently, Takahashi *et al* [7] have assessed the superconductivity of an iron-based quasi-1D compound $BaFe_2S_3$ under high pressure generated in a diamond anvil cell (DAC) and a cubic anvil press, and found that this compound exhibited a metal-insulator transition at about 11 GPa. Motivated by this discovery, tremendous research efforts have been focused on the structural, magnetic and superconductive properties of $BaFe_2S_3$ and opened up an interdisciplinary research field.

Arita *et al* [8] have studied the electronic structure of $BaFe_2S_3$ from the first principles calculations, and analyzed the full Fe orbital model, which revealed that the Fermi surfaces are represented only by the two Fe orbitals, i.e. w_{xz} and

$w_{x^2-y^2}$. They have also suggested that the superconductivity is mediated by spin fluctuations. Suzuki *et al* [9] have studied the magnetic, structural and electronic properties of $BaFe_2S_3$ based on density functional theory (DFT) with the generalized gradient approximation (GGA). Their results indicated that the applied pressure strongly suppressed the energy gap and leaded to an insulator-metal transition. Yamauchi *et al* [10] have performed high pressure study of $BaFe_2S_3$, by measuring dc-resistivity and ac-susceptibility up to 15 GPa. They have found that the antiferromagnetic insulating state at the ambient pressure could transformed into a metallic state at the critical pressure of 10 GPa. The metal-insulator transition boundary of $BaFe_2S_3$ terminates at a critical point around 10 GPa and 75 K. Using neutron diffraction, Chi *et al* [11] have studied the pressure effects on the antiferromagentic orders in iron-based ladder compound $BaFe_2S_3$. They have confirmed that $BaFe_2S_3$ undergoes a quantum phase transition where an abrupt increase of Néel temperature by more than 50% occurs at about 1 GPa, accompanied by a jump in the ordered moment. Wang *et al* [12] have measured the spin wave spectra of a $BaFe_2S_3$ powder sample using the inelastic neutron scattering, and demonstrated that the antiferromagnetic spin excitations are a common characteristic for the iron-based superconductors. Using the x-ray absorption and resonant inelastic x-ray scattering spectroscopy, Takubo *et al* [13] have studies the electronic structure of $BaFe_2X_3$ (X = S and Se) and $CsFe_2Se_3$. They have revealed that the direct exchange interaction along the legs of the Fe ladder stabilizes the orbital and antiferromagnetic orders in $BaFe_2S_3$.

Although numerous studies are reported on $BaFe_2S_3$, very little is known on the structural evolution and electronic properties of $BaFe_2S_3$ under high pressure, especially above 20 GPa. Several important questions about $BaFe_2S_3$ are still unanswered: (1) As the pressure increases, will structural phase transition occur and produce new phases? (2) What are their structural properties? (3) Are these phases semiconducting or metallic phases? To answer these questions, we here report an extensive structure search based on the Crystal structure AnaLYsis by Particle Swarm Optimization (CALYPSO) structure search method combined with first-principles calculations. The paper is organized as follows: In section 2, a brief description of the theory and method details are displayed. The calculated structural and electronic properties are discussed in section 3. Conclusions are summarized in section 4.

2. Computational methods

The structure search of $BaFe_2S_3$ are performed by using an unbiased structure search method based on the particle swarm optimization algorithm as implemented in the CALYPSO code [14, 15], which has the capability of finding stable or metastable structures with only the knowledge of the chemical composition at given external conditions (for example, pressure) as input. The efficiency of this method has been demonstrated on a variety of systems, ranging from elements to binary and ternary compounds [16–26]. In the present work, the evolutionary variable-cell structure predictions are performed using unit cells containing up to four formula units and at pressures of 0, 10, 20, 50, 100 GPa. In the first step, random structures with certain symmetry are constructed in which atomic coordinates are generated by the crystallographic symmetry operations. Each generation of trial structures contains 30 candidates, 70% of the structures are generated by the particle swarm optimization, while the other 30% will be generated randomly; 50 generations are followed to achieve the converged structures. The geometry optimization and electronic structure calculations are carried out in the framework of DFT using the Perdew–Burke–Ernzerh functional with exchange and correlation treated within the GGA [27] as implemented in the Vienna *ab initio* simulation package (VASP) [28]. The projector augmented wave [29] method is adopted with $5s^25p^66s^2$, $3d^54s^2$ and $3s^23p^4$ treated as valence electrons for Ba, Fe and S atoms, respectively. To obtain reliable results, we have chosen a kinetic cutoff energy of 800 eV and appropriate Monkhorst–Pack *k*-meshes with a grid spacing of 0.02 $Å^{-1}$ to ensure the convergence of total energy calculations within 1 meV/atom. The phonon dispersion curves are calculated by using a supercell approach as implemented in the PHONOPY code [30]. The electron localization functions (ELF) [31, 32] are calculated by VASP and plotted by using the VESTA software [33].

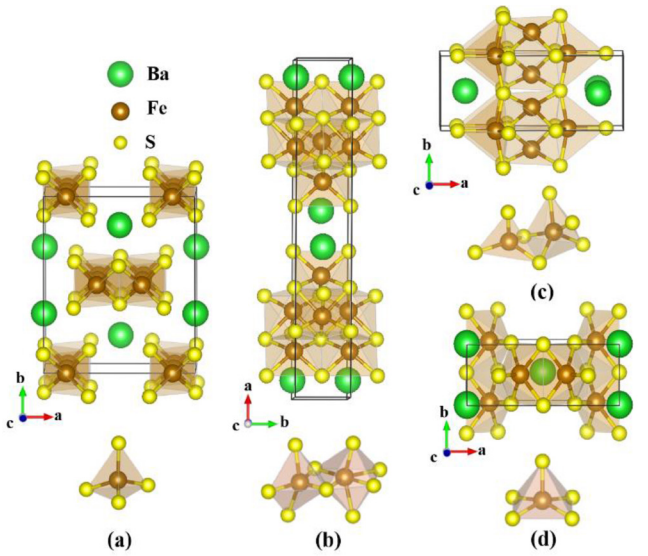

Figure 1. The selected stable phases for $BaFe_2S_3$. (a) Structure of *Cmcm* at 12 GPa. (b) Structure of *C*2/*m* at 100 GPa. (c) Structure of $P222_1$ at 40 GPa. (d) Structure of *Imm*2 at 50 GPa.

3. Results and discussion

To explore the structure evolution of $BaFe_2S_3$ under high pressure, we have performed extensively structural searches of $BaFe_2S_3$ at the pressure range of 0–100 GPa. Ultimately, we have obtained eight low-energy candidates with space groups $P222_1$, $P2_1$, *Imm*2, *C*2/*m*, *Pm*, *Pmmm*, *C*2/*c*, and *Cmcm* [7],

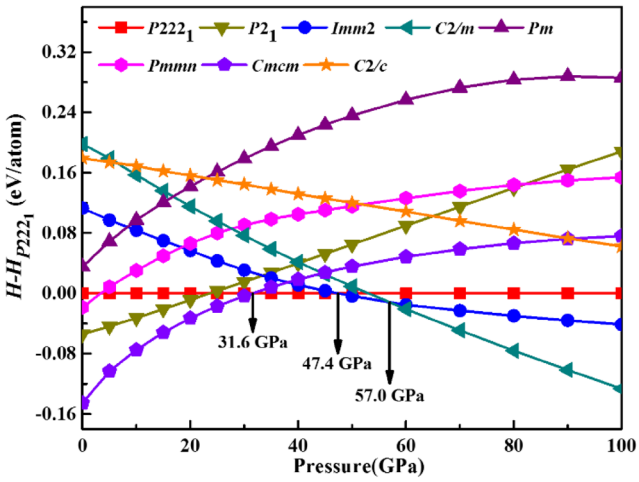

Figure 2. Enthalpy-pressure relations of $BaFe_2S_3$. The enthalpies are shown per atom and relative to the $P222_1$ phase.

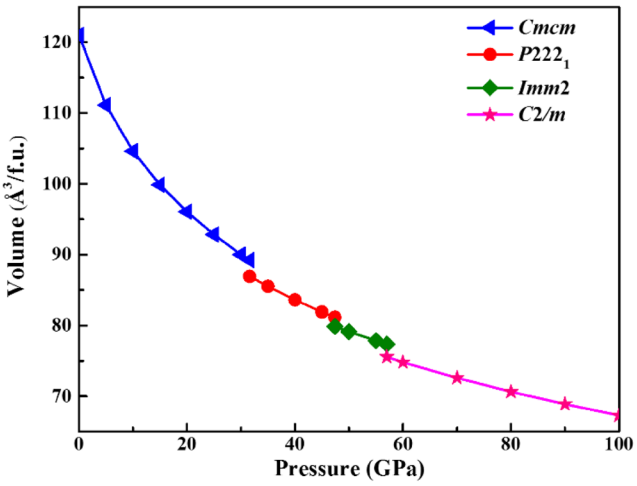

Figure 3. Volume per formula unit for $BaFe_2S_3$ as a function of pressure.

which are depicted in figures 1 and S1 (see the supporting information at stacks.iop.org/JPhysCM/31/115401/mmedia), from 1500 structures of $BaFe_2S_3$ through the structure searches. The structural information of $BaFe_2S_3$ at ambient pressure, including the lattice parameters and atomic coordinates, are listed in table S1 (see the supporting information), together with the available experimental values [7] for comparison. It can be seen from table S1 that our calculated lattice parameters of *Cmcm* phase are in good agreement with the experiment values, which give us confidence in the applicability of the calculated method to $BaFe_2S_3$.

The enthalpy-pressure relations of the selected candidate structures are plotted in figure 2. From figure 2, we can seethat, the *Cmcm* phase is the most stable structure at ambient pressure, which is accorded well with the result of experiment [7]. For *Cmcm* phase at 12 GPa, the atomic positions of Ba (4c), Fe (8e), S (4c), and S (8g) are (0.500, 0.161, 0.750), (0.339, 0.500, 0.500), (0.500, 0.639, 0.750) and (0.192, 0.352, 0.750), respectively. Each Fe atoms are surrounded by four nearest neighboring S atoms, which form a tetrahedron (see figure 1). Fe atoms in *Cmcm* phase exhibit four-fold coordination of S atoms. The *Cmcm* phase is stable up to about 31.6 GPa, and then transforms into $P222_1$ phase. In $P222_1$ phase, one Ba atom locates at 2b (0.137, 0.500, 0.500) site, two Fe atoms occupy on two inequivalent Wyckoff sites 2a (0.303, 0.000, 1.000) and 2d (0.500, 0.700, 1.250), and three S atoms locate at 2a (0.093, 0.000, 1.000), 2a (0.369, 0.000, 0.500) and 2b (0.343, 0.500, 1.000) positions. Interestingly, Fe atoms in this orthorhombic $P222_1$ phase exhibit mixed four-fold and five-fold coordination of S atoms. With further pressure increasing, the $P222_1$ phase transforms into *Imm*2 phase at 47.4 GPa. In *Imm*2 phase, each Fe atom is 5-fold coordinated with S atom. Fe atom occupy on the 4d site (0.500, 0.651, 0.158), S atom occupy on the 4d sites (0.500, 0.208, 0.875) and 2b sites (0.000, 0.500, 0.027), while Ba atom locates on the 2a site (0.000, 0.000, 0.145). Upon further compression, *Imm*2 phase transforms into *C*2/*m* phase at 57.0 GPa, which is stable up to at least 100 GPa. The *C*2/*m* phase contains one Ba atom occupied on the 4i site (0.445, 0.500, 0.773), two Fe atom occupied on the 4i at (0.241, 0.500, 0.707) and (0.362, 0.500, 0.351), and three S atoms also occupied on the 4i at (0.195, 0.000, 0.965), (0.325, 0.000, 0.635) and (0.565, 0.00, 0.741), respectively. From figure 1, we can see that each Fe atom in the *C*2/*m* phase is surrounded by 5 or 6 S atoms. Significantly, the coordination of Fe atom in $BaFe_2S_3$ change from four-fold coordinated S atoms (*Cmcm*) to mixed four and five-fold coordinated S atoms ($P222_1$), and then to five-fold coordinated S atoms (*Imm*2), and further mixed five and six-fold coordinated S atoms (*C*2/*m*).

At 0 K, the *Cmcm* phase is the most stable structure at ambient pressure and then transforms into $P222_1$ phase at 31.6 GPa. Upon further compression, the $P222_1$ phase transforms into *Imm*2 phase at 47.4 GPa, which remains the most stable phase up to 57.0 GPa, and then transforms into *C*2/*m* phase. However, the three intermediate phases of $BaFe_2S_3$, *Cmcm*, $P222_1$ and *Imm*2, have very similar energies around 40 GPa. Some of them maybe not observed experimentally, as there are many other important features, for example, vibrational, temperature and kinetic effects. Some of them maybe coexist in an even wider range of pressure [34]. Thus, more work is needed to gain insight regarding their phase boundaries, which is an interesting topic for further study. The calculated pressure dependence of unit-cell volume of $BaFe_2S_3$ are presented in figure 3. We can find that *Cmcm* $\rightarrow$ $P222_1$ $\rightarrow$ *Imm*2 $\rightarrow$ *C*2/*m* phase transitions are discontinuous changes in volume at the transition pressure points, which indicate that the three transitions are first order phase transitions.

To determine the thermodynamic stability of $BaFe_2S_3$, we have optimized the structures of *Cmcm* phase and three other new phases of $P222_1$, *Imm*2 and *C*2/*m*, and calculated the formation enthalpies of $BaFe_2S_3$ under high pressure. The formation enthalpy per atom ΔH is calculated by using the reaction route as $\Delta H = [H(BaFe_2S_3) - H(Ba) - 2 * H(Fe) - 3 * H(S)]/6$, H represents the enthalpy per formula unit of the most stable structure for each composition at a specific pressure. The optimized lattice parameters and formation enthalpies of *Cmcm*, $P222_1$, *Imm*2 and *C*2/*m* phases for $BaFe_2S_3$ at considered pressures are listed in table 1. It can be seen from table 1 that the formation enthalpies of the four phases are negative, which indicate the four phases of $BaFe_2S_3$ are thermodynamically stable.

Table 1. Predicted lattic constants (Å, deg), atomic coordinates (fractional) and relative formation enthalpy (eV) per atom as referred to the conventional unit cells of *Cmcm* phase at 12 GPa, $P222_1$ phase at 40 GPa, *Imm*2 phase at 50 GPa and *C*2/*m* phase at 100 GPa.

Phase	Lattice constants	Atomic coordinates	ΔH
Cmcm	$a = 7.391$	Ba 4c(0.500, 0.161, 0.750)	−1.125
	$b = 7.676$	Fe 8e(0.339, 0.500, 0.500)	
	$c = 4.703$	S 4c(0.500, 0.639, 0.750)	
	$a = \beta = \gamma = 90$	S 8g(0.192, 0.352, 0.750)	
$P222_1$	$a = 10.041$	Ba 2b(0.137, 0.500, 0.500)	−1.305
	$b = 4.101$	Fe 2a(0.303, 0.000, 1.000)	
	$c = 4.062$	Fe 2d(0.500, 0.700, 1.250)	
	$\alpha = \beta = \gamma = 90$	S 2a(0.093, 0.000, 1.000)	
		S 2a(0.369, 0.000, 0.500)	
		S 2b(0.343, 0.500, 1.000)	
*Imm*2	$a = 3.151$	Ba 2a(0.000, 0.000, 0.145)	−1.326
	$b = 8.295$	Fe 2a(0.500, 0.651, 0.158)	
	$c = 6.054$	S 4d(0.500, 0.208, 0.875)	
	$\alpha = \beta = \gamma = 90$	S 2b(0.000, 0.500, 0.027)	
*C*2/*m*	$a = 18.474$	Ba 4i(0.445, 0.500, 0.773)	−1.353
	$b = 3.030$	Fe 4i(0.241, 0.500, 0.707)	
	$c = 4.851$	Fe 4i(0.362, 0.500, 0.351)	
	$\alpha = \gamma = 90$	S 4i(0.195, 0.000, 0.965)	
	$\beta = 82.6$	S 4i(0.325, 0.000, 0.635)	
		S 4i(0.565, 0.000, 0.741)	

To provide more guidelines for future experimental synthesis,we have simulated the x-ray diffraction (XRD) spectra of $BaFe_2S_3$. We show in figure 4 the calculated XRD spectra of the four phases of $BaFe_2S_3$ at ambient pressure and 12 GPa, we can see that the simulated XRD spectra of *Cmcm* phase overall agree with the measured XRD spectra of *Cmcm* phase, again validating our structure search and DFT calculated method in application to $BaFe_2S_3$. Moreover, it is easy to find that the simulated XRD spectra of $P222_1$, *Imm*2 and *C*2/*m* phases are sufficiently distinct from the experimental observed *Cmcm* phase. Thus, the three new phases of $BaFe_2S_3$ can be easily experimental identified with the current high pressure capability of diamond anvil cells (DAC). However, at high pressure, there is no available XRD data compared with our calculations. Experimental data of $BaFe_2S_3$ based on the DAC is needed to accurately determine their true structures.

In order to study the mechanical stability of $BaFe_2S_3$, we have calculated the elastic constants by using the stress–strain relations. The results are listed in table 2. The *Cmcm*, $P222_1$ and *Imm*2 phases of $BaFe_2S_3$ are all orthorhombic structures, which have nine independent elastic constants of C_{11}, C_{22}, C_{33}, C_{44}, C_{55}, C_{66}, C_{12}, C_{13} and C_{23}, and the correspond mechanical stability criteria are given by [35]:

$$C_{11} > 0, C_{22} > 0, C_{33} > 0, C_{44} > 0, C_{55} > 0, C_{66} > 0,$$
$$[C_{11} + C_{22} + C_{33} + 2(C_{12} + C_{13} + C_{23})] > 0,$$
$$(C_{11} + C_{22} - 2C_{12}) > 0, (C_{11} + C_{33} - 2C_{13}) > 0,$$
$$(C_{22} + C_{33} - 2C_{23}) > 0.$$

The *C*2/*m* phase is a monoclinic structure, which has thirteen independent elastic constants C_{11}, C_{22}, C_{33}, C_{44}, C_{55}, C_{66},

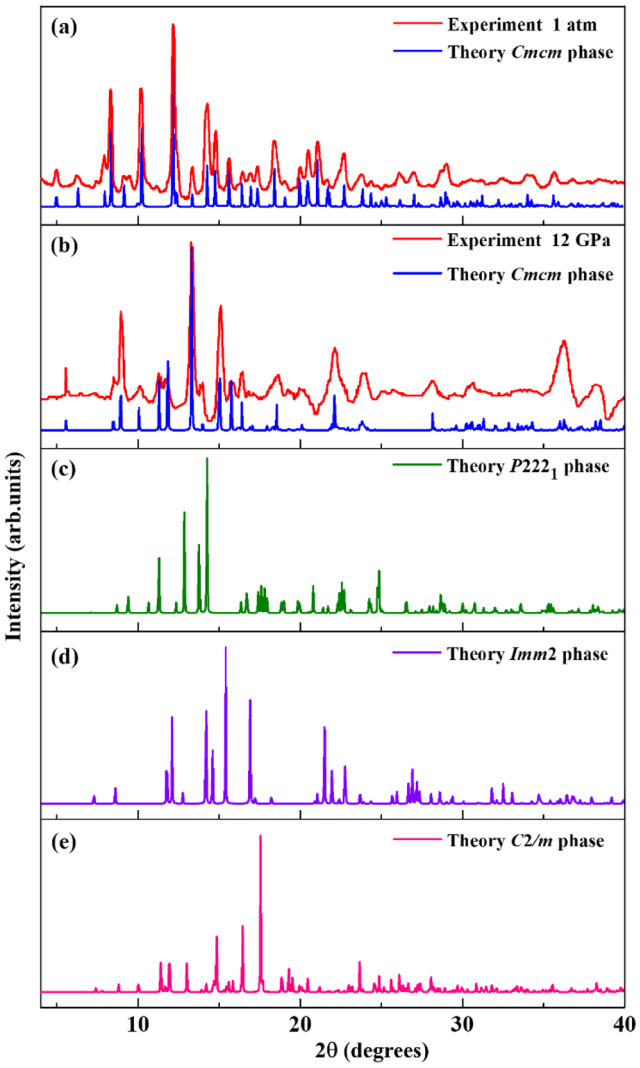

Figure 4. The experimental and simulated XRD patterns of $BaFe_2S_3$. (a) *Cmcm* phase at ambient pressure, (b) *Cmcm* phase at 12 GPa, (c) $P222_1$ phase at 40 GPa, (d) *Imm*2 phase at 50 GPa, and (e) *C*2/*m* phase at 100 GPa.

Table 2. Calculated elastic constants C_{ij} (GPa) and sound velocities of *Cmcm* phase at 12 GPa, $P222_1$ phase at 40 GPa, *Imm*2 phase at 50 GPa and *C*2/*m* phase at 100 GPa.

	Cmcm	$P222_1$	*Imm*2	*C*2/*m*
C_{11}	143.00	296.28	370.06	591.73
C_{22}	114.10	372.94	365.39	578.08
C_{33}	273.68	336.35	412.35	595.29
C_{44}	40.43	124.17	134.71	173.17
C_{55}	61.13	87.68	178.05	78.55
C_{66}	42.31	76.69	112.94	242.28
C_{12}	66.62	188.10	209.71	414.98
C_{13}	74.73	161.27	291.93	276.82
C_{23}	59.98	183.08	242.68	327.90
C_{15}				20.40
C_{25}				11.37
C_{35}				16.19
C_{46}				−45.22
V_P	5.38	7.09	7.66	8.38
V_S	2.92	3.57	3.75	3.97

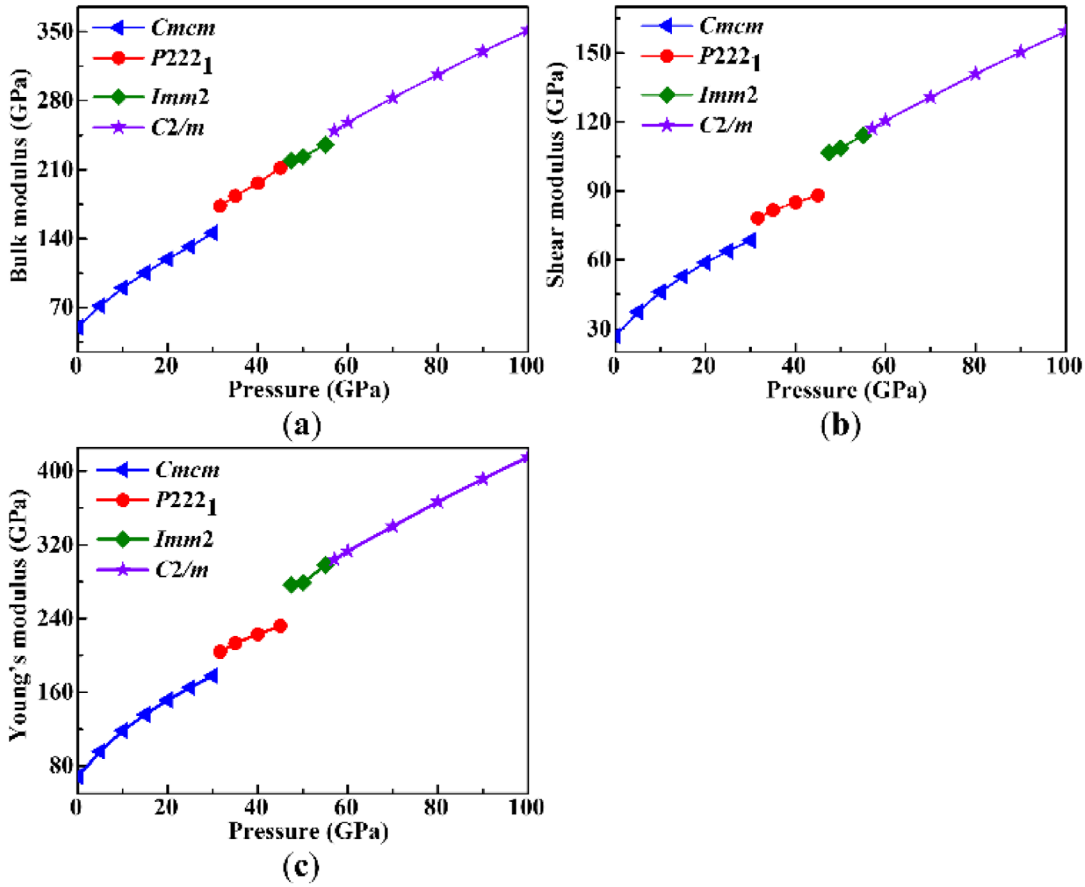

Figure 5. Calculated (a) bulk modulus B (b) shear modulus G and (c) Young's modulus E of $BaFe_2S_3$ at different pressures.

C_{12}, C_{13}, C_{23}, C_{15}, C_{25}, C_{35} and C_{46}, and the elastic constants should satisfy the following inequalities [35]:

$$C_{11} > 0, C_{22} > 0, C_{33} > 0, C_{44} > 0, C_{55} > 0, C_{66} > 0,$$
$$(C_{22} + C_{33} - 2C_{23}) > 0, (C_{33}C_{55} - C_{35}^2) > 0, (C_{44}C_{66} - C_{46}^2) > 0,$$
$$[C_{11} + C_{22} + C_{33} + 2(C_{12} + C_{13} + C_{23})] > 0,$$
$$[C_{22}(C_{33}C_{55} - C_{35}^2) + 2C_{23}C_{25}C_{35} - C_{23}^2C_{55} - C_{25}^2C_{33}] > 0,$$
$$2[C_{15}C_{25}(C_{33}C_{12} - C_{13}C_{23}) + C_{15}C_{35}(C_{22}C_{13} - C_{12}C_{23})$$
$$+C_{25}C_{35}(C_{11}C_{23} - C_{12}C_{13})] - [C_{15}^2(C_{22}C_{33} - C_{23}^2)$$
$$+C_{25}^2(C_{11}C_{33} - C_{13}^2) + C_{35}^2(C_{11}C_{22} - C_{12}^2)]$$
$$+C_{55}C_{11}C_{22}C_{33} - C_{11}C_{23}^2 - C_{22}C_{13}^2 - C_{33}C_{12}^2 + 2C_{12}C_{13}C_{23} > 0.$$

The calculated elastic constants, shown in table 2, clearly reveal that the four phases of $BaFe_2S_3$ at the considered pressures satisfy the mechanical stable criteria, confirming their mechanical stability.

To probe the pressure dependence physical behavior of $BaFe_2S_3$, we have calculated elastic constants depending on pressure. From the calculated elastic constants, we can obtain the bulk modulus B, shear modulus G and Young's modulus E of $BaFe_2S_3$ at high pressure by using the Voigt–Reuss–Hill method. The results are illustrated in figure 5. From figure 5, we can observe that the bulk modulus, shear modulus and Young's modulus of $BaFe_2S_3$ all increase monotonically with the increasing pressure. In addition, we can separate the ductile and brittle materials from the critical value of B/G, which is about 1.75. The four phases of $BaFe_2S_3$ at high pressure all have the B/G ratio values larger than 1.75, indicating their ductile nature.

To further validate the dynamical stability of $BaFe_2S_3$, we have calculated the phonon dispersion curves along the high-symmetry directions of the Brillouin zones for *Cmcm* phase at 12 GPa, $P222_1$ phase at 40 GPa, *Imm*2 phase at 50 GPa, and *C*2/*m* phase at 100 GPa, respectively. The calculated phonon dispersion curves are illustrated in figure 6. In fact, according to phonon theory [30], a solid phase with negative phonon frequencies would be unstable and tend to transform to a lower energy structure. However, if a system is located at its local minima on the potential energy surface, no negative frequencies will appear. As shown in figure 6, no imaginary frequencies modes are found in the whole Brillouin zones, indicating that the four phases of $BaFe_2S_3$ are dynamically stable at the given pressures.

To gain a deeper understanding of the electronic properties of $BaFe_2S_3$ under high pressure, we have calculated the electronic band structure and the density of states of $BaFe_2S_3$ at different pressures. The calculated results are shown in figure 7. From figure 7, we can see that all the phases of $BaFe_2S_3$ at the given pressures exhibit metallic character due to the finite electronic DOS at the Fermi level. In addition, the projected DOS show that the four phases of $BaFe_2S_3$ have the similar electronic distributions and the total DOS are largely contributed by 3*d* states of Fe atoms and 3*p* states of S atoms,

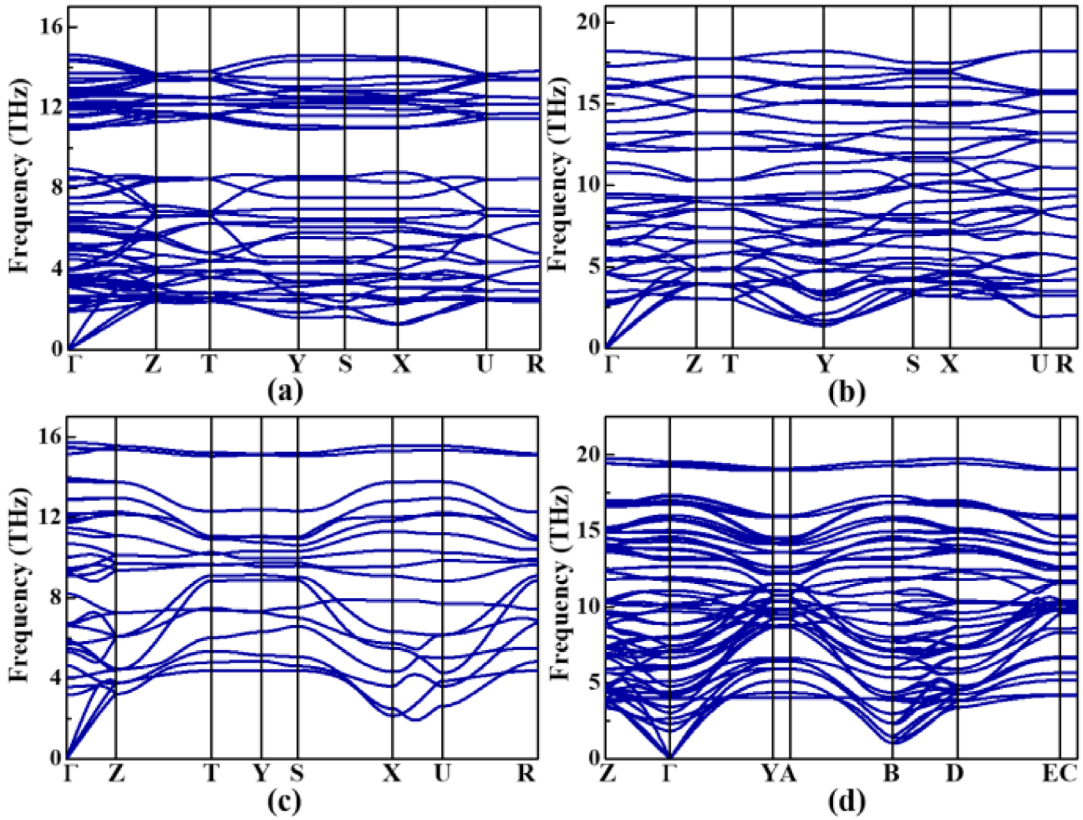

Figure 6. Calculated phonon dispersions of $BaFe_2S_3$ under high pressure. (a) *Cmcm* phase at 12 GPa, (b) $P222_1$ phase at 40 GPa, (c) *Imm*2 phase at 50 GPa, and (d) *C*2/*m* phase at 100 GPa.

while both the *p* and *s* states of Ba atoms make a negligible contribution to the total DOS at whole levels.

To visualize the bonding character in $BaFe_2S_3$, we have calculated the ELF of the four phases at the considered pressures. The results are depicted in figure 8. The strong covalent bonding between Fe atoms and neighboring S atoms in the four phases of $BaFe_2S_3$ can be seen from the ELF. Furthermore, we have also assessed charge distribution in $BaFe_2S_3$ by computing the Bader charges using the atom in molecules approach [36]. The calculated results are listed in table 3. From table 3, we can see that the partial charges of *Cmcm* phase at 12 GPa are +1.40 *e* and +0.48 *e* for Ba and Fe atoms and −0.79 *e* for S atoms, respectively. As for the $P222_1$ phase at 40 GPa, the corresponding values are +1.25 *e* and +0.44 *e* for Ba and Fe atoms and −0.71 *e* for S atoms. For the *Imm*2 phase under 50 GPa, the Ba atoms and Fe atoms are positively charged with +1.13 *e* and +0.47 *e*, while the S atoms are negatively charged with −0.69 *e*. In the *C*2/*m* structure at 100 GPa, Ba atoms and Fe atoms are positively charged with +1.05 *e* and +0.40 *e*, while S atoms are negatively charged with −0.62 *e*. These results seem to suggest that the similar amounts of charge transfer in all the four phases of $BaFe_2S_3$ at different pressures.

Ba, Fe and S are common elements, which are widely distributed in Earth's surface and interior. The sound velocity behaviors of related compounds, composing by Ba, Fe and S elements, are important for understanding the evolution processes in the Earth's crust and upper mantle. In order to establish the complete shape of anisotropy and understand the evolution of seismic anisotropy of $BaFe_2S_3$ as a function of pressure, we have calculated *P*-wave velocity (V_P) and *S*-wave velocity (V_S) of the four phases under high pressure. The obtained sound velocities are also listed in table 2. The percentage of *P*-wave and *S*-wave anisotropies are defined as $AV_X = 100\% \times (V_{X\max} - V_{X\min})/[(V_{X\max} + V_{X\min})/2]$ ($X = P$, *S*) [34, 37]. Selected sound-velocity profiles of *Cmcm* phase at 12 GPa, $P222_1$ phase at 40 GPa, *Imm*2 phase at 50 GPa, and *C*2/*m* phase at 100 GPa, are shown in figure 9. It can be seen from figure 9(a) that the extremal *P*-wave propagations of *Cmcm* under 12 GPa occur in the basal plane with the fastest velocity ($V_{P\max} = 7.00$ km s^{-1}) in the ⟨0 0 1⟩ direction and the slowest ($V_{P\min} = 4.52$ km s^{-1}) in the ⟨0 1 0⟩ direction. The corresponding AV_P and AV_S are 43.06% and 28.60%, respectively. In contrast to the *Cmcm* phase, the three new phases ($P222_1$, *Imm*2, and *C*2/*m*) show drastically different sound velocity profiles. Under 40 GPa, the fastest *P*-wave of $P222_1$ ($V_{P\max} = 7.59$ km s^{-1}) distribute in the ⟨0 3 1⟩ direction and the slowest *P*-wave ($V_{P\min} = 6.57$ km s^{-1}) propagates along with the $\langle \bar{1}\,0\,0 \rangle$ direction, with an AV_P of 14.38% (see figure 9(b)). The fastest velocity of *Imm*2 at 50 GPa is 8.48 km s^{-1}

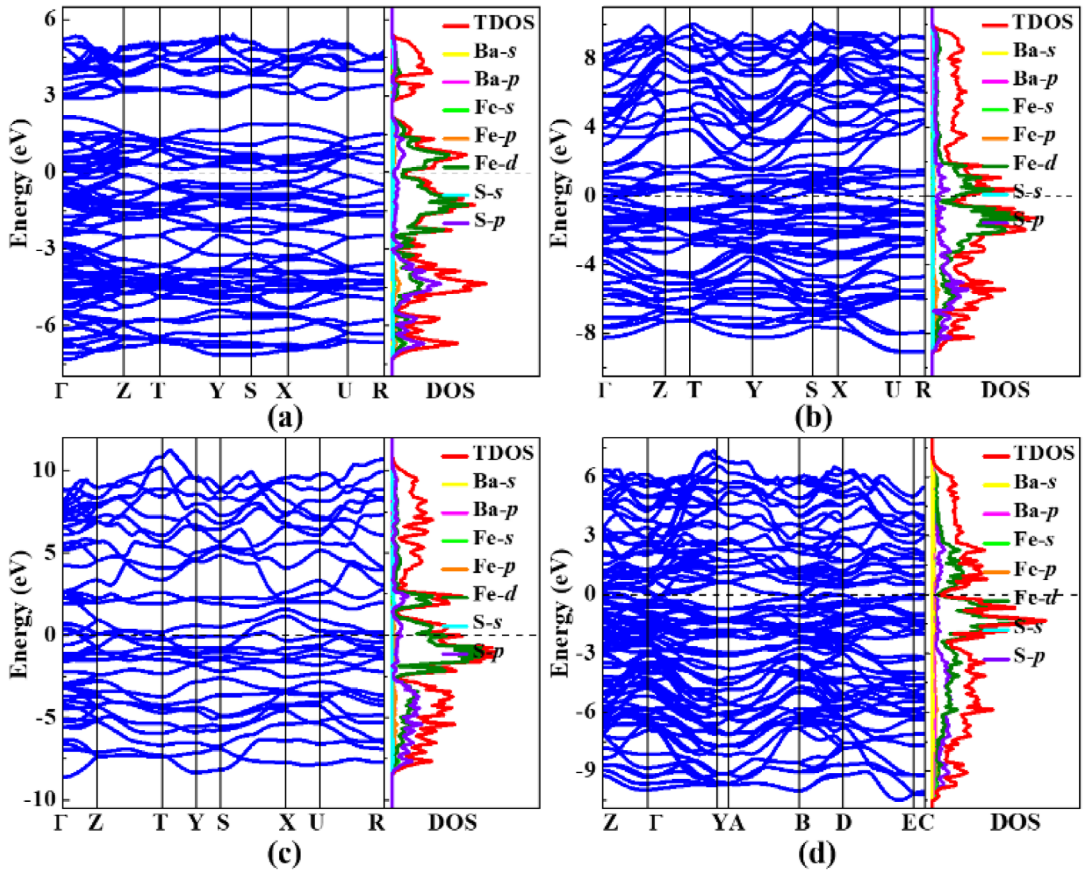

Figure 7. Calculated electronic band structures density of states of $BaFe_2S_3$ under high pressure. (a) *Cmcm* phase at 12 GPa, (b) $P222_1$ phase at 40 GPa, (c) *Imm*2 phase at 50 GPa, and (d) *C*2/*m* phase at 100 GPa.

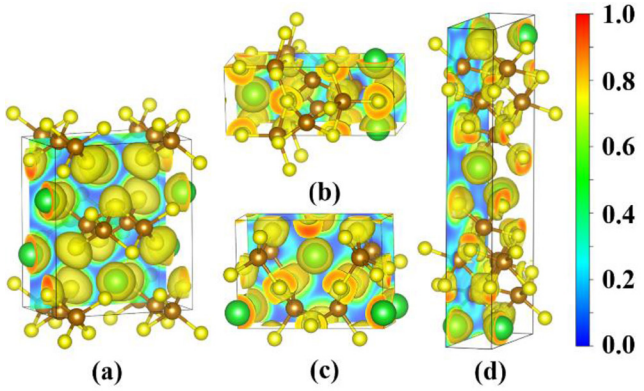

Figure 8. ELF of $BaFe_2S_3$ under high pressure. (a) *Cmcm* phase at 12 GPa, (b) $P222_1$ phase at 40 GPa, (c) *Imm*2 phase at 50 GPa, and (d) *C*2/*m* phase at 100 GPa. The ELF isosurfaces value is 0.75.

Table 3. Calculated Bader charges of *Cmcm* phase at 12 GPa, $P222_1$ phase at 40 GPa, *Imm*2 phase at 50 GPa and *C*2/*m* phase at 100 GPa. ω is the charge transfer from Ba or Fe to a S atom.

Phase	atom	Charge value (e)	ω (e)
Cmcm	Ba	8.60	1.40
	Fe	7.52	0.48
	S	6.79	−0.79
$P222_1$	Ba	8.75	1.25
	Fe	7.56	0.44
	S	6.71	−0.71
*Imm*2	Ba	8.87	1.13
	Fe	7.53	0.47
	S	6.69	−0.69
*C*2/*m*	Ba	8.95	1.05
	Fe	7.60	0.40
	S	6.62	−0.62

in the $\langle 1\,0\,1\rangle$ direction and the slowest velocity is 7.10 km s^{-1} in the $\langle 0\,1\,0\rangle$ direction (see figure 9(c)), respectively. Remarkably, the fastest and slowest V_P of *C*2/*m* phase at 100 GPa are 9.36 km s^{-1} in the $\langle \bar{1}\,1\,0\rangle$ direction and 7.48 km s^{-1} in the $\langle \bar{1}\,0\,1\rangle$ direction, respectively with a AV_P of 22.31% (see figure 9(d)). The maximum *S*-wave anisotropy is 55.90% in the $\langle \bar{1}\,0\,1\rangle$ direction, which increases by double compared to the *Cmcm* phase. The fascinating sound velocity behaviors in the four phases of $BaFe_2S_3$ under high pressure provide useful information for interpreting the evolution processes in the Earth. However, up to now, no experimental data are available for comparison, and further experimental work is required.

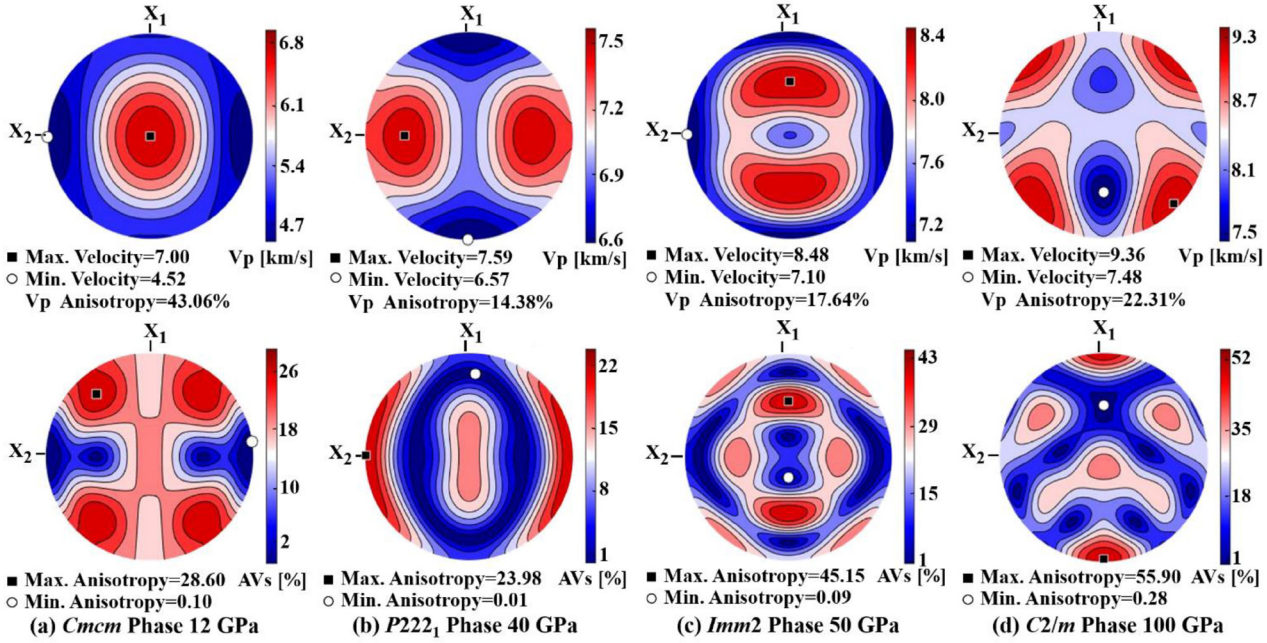

Figure 9. Stereographic projections of calculated *P*-wave velocity V_P (in km s^{-1}) and *S*-wave anisotropy AV_S (in %) of $BaFe_2S_3$ under high pressure. (a) *Cmcm* phase at 12 GPa, (b) $P222_1$ phase at 40 GPa, (c) I*mm*2 phase at 50 GPa, and (d) *C*2/*m* phase at 100 GPa. The coordinate axes are $X_1 = [1\,0\,0]$, $X_2 = [0\,1\,0]$, $X_3 = [0\,0\,1]$. The black square and the white circle indicate the maximum and minimum velocities.

4. Conclusion

In summary, we have performed a comprehensive computational study of $BaFe_2S_3$ under high pressure by CALYPSO structural search method and first-principles calculations. We have uncovered three intriguing $P222_1$, *Imm*2 and *C*2/*m* phases of $BaFe_2S_3$ at 0 K under high pressure. Our results indicate that $BaFe_2S_3$ undergoes a structural phase transition of *Cmcm* → $P222_1$ → *Imm*2 → *C*2/*m* with the transition pressures around 31.6, 47.4 and 57.0 GPa, respectively. Accurate elastic constants and phonon dispersion curves of $BaFe_2S_3$ show that the four phases are mechanically and dynamically stable at dominating pressures. The large variations of the sound velocity behaviors in the four phases at different pressures provide insights for interpreting the seismic signatures of $BaFe_2S_3$ under high pressure. We hope that the three new phases of $BaFe_2S_3$ can be experimentally identified with future high pressure experiments.

Acknowledgments

This work was supported by the National Natural Science Foundation of China (Nos. U1804121, 11304167, 11604175, 21671114, 11747139 and 11804031), the NSAF (No. U1530402), the 973 Program of China (No. 2014CB660804), the Special Program for Applied Research on Super Computation of the NSFC-Guangdong Joint Fund (the second phase No. U1501501), the Program for Science & Technology Innovation Talents in Universities of Henan Province (No. 15HASTIT020), and the Science and Technology Plan Projects of Qinghai province (No. 2014-ZJ-942Q). Parts of the calculations were performed using the Cherry Creek Supercomputer of the UNLV's National Supercomputing Institute.

Supplementary information

See supplementary material for the predicted crystal structures of *P*21, *Pm*, *Pmmn* and *C*2/*c* phases, optimized lattice constants and atomic coordinates of $BaFe_2S_3$ under ambient pressure at 0 K.

ORCID iDs

Panlong Kong https://orcid.org/0000-0003-2164-4836

References

[1] Popović Z V, Šćepanović M, Lazarević N, Opačić M, Radonjić M M, Tanasković D, Lei H C and Petrovic C 2015 *Phys. Rev.* B **91** 064303
[2] Krzton-Maziopa A, Shermadini Z, Pomjakushina E, Pomjakushin V, Bendele M, Amato A, Khasanov R, Luetkens H and Conder K 2011 *J. Phys.: Condens. Matter* **23** 052203
[3] Kamihara Y, Watanabe T, Hirano M and Hosono H 2008 *J. Am. Chem. Soc.* **130** 3296–7
[4] Jiang S, Xing H, Xuan G F, Wang C, Ren Z, Feng C M, Dai J H, Xu Z A and Cao G H 2009 *J. Phys.: Condens. Matter* **21** 382203
[5] Lumsden M D and Christianson A D 2010 *J. Phys.: Conders. Matter* **22** 203203
[6] Dai P C, Hu P J and Dagotto E 2012 *Nat. Phys.* **8** 709–18
[7] Takahashi H *et al* 2015 *Nat. Mater.* **14** 1008–12
[8] Arita R, Ikeda H, Sakai S and Suzuki M T 2015 *Phys. Rev.* B **92** 054515
[9] Suzuki M T, Arita R and Ikeda H 2015 *Phys. Rev.* B **92** 085116
[10] Yamauchi T, Hirata Y, Ueda Y and Ohgushi K 2015 *Phys. Rev. Lett.* **115** 246402

[11] Chi S, Uwatoko Y, Gao H, Hirata Y, Hashizume K, Aoyama T and Ohgushi K 2016 *Phys. Rev. Lett.* **117** 047003
[12] Wang M, Jin S J, Yi M, Song Y, Jiang H C, Zhang W L, Sun H L and Luo H Q 2017 *Phys. Rev.* B **95** 060502
[13] Takubo K *et al* 2017 *Phys. Rev.* B **96** 115157
[14] Wang Y C, Lv J, Zhu L and Ma Y M 2010 *Phys. Rev.* B **82** 094116
[15] Wang Y C, Lv J, Zhu L and Ma Y M 2012 *Comput. Phys. Commun* **183** 2063–70
[16] Lv J, Wang Y C, Zhu L and Ma Y M 2011 *Phys. Rev. Lett.* **106** 015503
[17] Zhu L, Liu H Y, Pickard C J, Zou G T and Ma Y M 2014 *Nat. Chem.* **6** 644–8
[18] Zhu L, Wang H, Wang Y C, Lv J, Ma M Y, Cui Q L, Ma Y M and Zou G T 2011 *Phys. Rev. Lett.* **106** 145501
[19] Li Y W, Hao J, Liu H Y, Li Y L and Ma Y M 2014 *J. Chem. Phys.* **140** 174712
[20] Wang H, Tse J S, Tanaka K, Iitaka T and Ma Y M 2012 *Proc. Natl Acad. Sci. USA* **109** 6463–6
[21] Zhou D, Li Q, Ma Y M, Cui Q L and Chen C F 2013 *J. Phys. Chem.* C **117** 5352–7
[22] Li Q, Zhou D, Zheng W T, Ma Y M and Chen C F 2013 *Phys. Rev. Lett.* **110** 136403
[23] Zhang M, Liu H Y, Li Q, Gao B, Wang Y C, Li H D, Chen C F and Ma Y M 2015 *Phys. Rev. Lett.* **114** 015502
[24] Li Q, Zhou D, Zheng W T, Ma Y M and Chen C F 2015 *Phys. Rev. Lett.* **115** 185502
[25] Zhou D, Li Q, Zheng W T, Ma Y M and Chen C F 2017 *Phys. Chem. Chem. Phys.* **19** 4560–6
[26] Lu C, Li Q, Ma Y M and Chen C F 2017 *Phys. Rev. Lett.* **119** 115503
[27] Perdew J P, Chevary J A, Vosko S H, Jackson K A, Pederson M R, Singh D J and Fiolhais C 1992 *Phys. Rev.* B **46** 6671–87
[28] Kresse G and Furthmuller J 1996 *Phys. Rev.* B **54** 11169–86
[29] Blochl P E 1994 *Phys. Rev.* B **50** 17953–79
[30] Togo A, Oba F and Tanaka I 2008 *Phys. Rev.* B **78** 134106
[31] Becke A D and Edgecombe K E 1990 *J. Chem. Phys.* **92** 5397–403
[32] Savin A, Jepsen O, Flad J, Andersen O K, Preuss H and von Schnering H G 1992 *Angew. Chem., Int. Ed. Engl.* **31** 187–8
[33] Momma K and Izumi F 2008 *J. Appl. Crystallogr.* **41** 653–8
[34] Lu C, Amsler M and Chen C F 2018 *Phys. Rev.* B **98** 054102
[35] Wu Z J, Zhao E J, Xiang H P, Hao X F, Liu X J and Meng J 2007 *Phys. Rev.* B **76** 054115
[36] Tang W, Sanville E and Henkelman G 2009 *J. Phys.: Condens. Matter* **21** 084204
[37] Mainprice D 1990 *Comput. Geosci.* **16** 385–93